Nanoscale

PAPER

Check for updates

Fatigue behavior of freestanding nickel–molybdenum–tungsten thin films with high-density planar faults†

JungHun Park, [iD] Yuhyun Park, Sunkun Choi, Zhuo Feng Lee and Gi-Dong Sim [iD] *

This research addresses the fatigue behavior of freestanding nickel–molybdenum–tungsten (Ni–Mo–W) thin films with high-density planar faults. The as-deposited Ni–Mo–W thin films demonstrate an unprecedented fatigue life, withstanding over a million cycles at a Goodman stress amplitude ($S_{a,Goodman}$) of 2190 MPa – nearly 80% of the tensile strength. The texture, columnar grain width, planar fault configuration (spacing and orientation), and tensile strength were unchanged after annealing at 500 °C for 24 hours, and the film endured over 2×10^5 cycles at $S_{a,Goodman}$ of 1050 MPa. The fatigue life of annealed Ni–Mo–W thin films is comparable to those of nanocrystalline Ni-based alloys, but has deteriorated significantly compared to that of the as-deposited films. The high fatigue strength of Ni–Mo–W thin films is ascribed to extremely dense planar faults suppressing fatigue crack initiation, and planar fault–dislocation interaction and grain boundary plasticity are proposed as mechanisms responsible for the fatigue failure. Provisionally the latter is a more convincing account of the experimental results, in which changes in the grain boundary characteristics after annealing cause higher susceptibility to stress concentration during cyclic loading. The fatigue behavior revealed in this work consolidates the thermal and mechanical reliability of Ni–Mo–W thin films for potential nano-structural applications.

Introduction

Steady growth of the micro-electromechanical system (MEMS) market has stimulated the demand for designing and fabricating more robust metallic thin films. Face-centered cubic (fcc) metals with intermediate to low stacking fault energy (SFE) have particularly garnered scientific attention due to their superior strength and thermal stability, previously unseen in conventional ultrafine-grained (ufg)/nanocrystalline (nc) counterparts.[1–10] The enhanced performance in these metals is attributed to the presence of nano-scale planar faults – twin boundaries (TBs) and stacking faults (SFs) – that arise from irregular stacking of close-packed atomic layers. Several studies have extensively investigated nanotwinned materials over the past few decades,[1–5,7,11–14] including explorations on the effect of TB spacing[1–3] and different combinations of grain morphology and the loading orientation.[15–18] It was also discovered that TBs possess high thermal stability and undergo minute coarsening, which is in stark contrast to the thermal response of conventional high-angle grain boundaries (GBs).[7,9]

Department of Mechanical Engineering, Korea Advanced Institute of Science and Technology 291, Daehak-ro, Yuseong-gu, Daejeon 34141, Republic of Korea.
E-mail: gdsim@kaist.ac.kr

Moreover, metals with high-density SFs were recently highlighted for their unique mechanical behavior that originates from SF–dislocation interactions.[19–24]

Nickel (Ni) is one of the most commercialized fcc metals in structural applications – from turbine blades to MEMS devices – owing to its resilience against corrosion and creep.[25,26] Strengthening Ni by introducing planar faults has been challenging due to its inherently high SFE, but recently Sim *et al.*[27,28] experimentally demonstrated that alloying Mo and W in Ni produces a microstructure with significant amounts of planar faults. Nickel–molybdenum–tungsten (Ni–Mo–W) films fabricated by sputter deposition displayed an unprecedented tensile strength (~3 GPa) and microstructural stability. Follow-up studies attempted to verify the potential of Ni–Mo–W thin film as a structural material by preparing the sample at a much lower deposition rate,[29,30] measuring the thermal expansion coefficient[31] and electrical resistance,[32] assessing the thermal stability with an *in situ* transmission electron microscopy (TEM) study,[33] and fabricating micro-cantilever beams.[34]

For a complete reliability evaluation, the fatigue resistance of Ni–Mo–W thin films must be understood. Repeated cyclic loading is responsible for more than half of the structural failures for components in service.[35] The same problem holds for small-scale devices such as radio frequency (rf) MEMS switches, which typically endure extremely high cycle fatigue

(10^9 cycles and beyond) during their service.[36] Despite the growing need for understanding the intrinsic fatigue behavior of thin films, there are only a limited number of studies that successfully performed such experiments.[37–40] The difficulties stem from handling the flimsy samples without a substrate, and controlling the cyclic load with high accuracy. This study addresses the fatigue behavior of freestanding submicron Ni–Mo–W thin films before and after heat treatment at 500 °C for 24 hours. As-deposited and annealed Ni–Mo–W thin films were tested under room temperature tension–tension fatigue loading. Microstructural analyses and relevant fatigue phenomena are discussed to understand the deformation mechanisms behind the fatigue behavior of planar-faulted Ni–Mo–W thin films.

Experimental procedures

Sample preparation

Ni–Mo–W thin films were deposited from a 2-inch diameter $Ni_{77.6}Mo_{20}W_{2.4}$ alloy target (nominal composition in atomic percent, 99.95% purity; Kurt J. Lesker) mounted on a direct-current (DC) magnetron sputtering system (J Vacuum Technology). The films were uniformly deposited on 200 μm-thick (100) silicon wafers, coated with low-pressure chemical vapor-deposited (LPCVD) silicon nitride layers on both sides. The DC power was set as 300 W, argon pressure and flow rate as 1 mTorr and 25 sccm respectively, and the base pressure was below 1×10^{-6} Torr. The deposited film was patterned in dog-bone shaped specimens *via* photolithography and wet-etching, followed by a series of reactive ion etching and bulk silicon etching (Fig. 1(a)) to render the test specimen freestanding as shown in the sky blue inset in Fig. 1(b). The gauge width of the dog-bone sample ranged from 100 to 200 μm, and the length ranged from 650 to 1950 μm. The average thickness of the fabri-

cated samples measured using a surface profiler (Tencor Alpha-step 500) approximated to 620 nm. Another batch of 680 nm-thick films was prepared using identical deposition parameters and patterning processes. The additionally fabricated freestanding films were annealed at 500 °C for 24 hours at a base pressure below 1.5×10^{-6} Torr. The residual stresses of the freestanding films were evaluated by conducting constant displacement rate membrane deflection experiment (MDE)[41–43] using strip-shaped freestanding Ni–Mo–W membranes that were fabricated along with the dog-bone shaped samples.[42] The residual stress of the as-deposited Ni–Mo–W thin films approximates to 430 MPa, and that of the annealed thin films approximates to 791 MPa (both of which are in tension).

Textural and microstructural characterization

The texture of Ni–Mo–W thin films was obtained from θ–2θ X-ray diffraction (XRD; RIGAKU SmartLab) at a 2θ range from 30° to 105°. The chemical composition was measured by energy dispersive spectroscopy (EDS) in a scanning electron microscope (SEM; Hitachi SU8230). The chemical composition of the unannealed batch was $Ni_{79.7}Mo_{18.0}W_{2.3}$, and that of the annealed batch was $Ni_{80.8}Mo_{18.1}W_{1.9}$ (both in atomic percent). Transmission electron microscopy (TEM) imaging was utilized to compare the microstructure before and after deformation. For TEM sample preparation, focused-ion beam (FIB) cross-section lift-out was conducted (ThermoFisher Helios G4 UX DualBeam) at the grip section to characterize the undeformed state, and near (a few μm to tens of μm away from) the fracture plane to characterize the deformed state. Bright-field TEM images were taken at an operating voltage of 200 kV (JEOL JEM-2100F HR) to identify the grain morphology and size, as well as the planar fault spacing and orientation. Lastly, the surface roughness of as-deposited and annealed Ni–Mo–W thin films was characterized by atomic force microscopy (AFM; INNOVA LAB-RAM HR800).

Mechanical testing

The details of the micro-mechanical tester (Fig. 1(c)) are elaborated in the ref. 44. As-fabricated specimens for tensile tests were first patterned with Al_2O_3 powder dispersed in ethanol (pink inset of Fig. 1(c)), so that the strain could be measured by tracking the relative displacement of the particles in the gauge section *via* digital image correlation (DIC).[45] Uniaxial tensile tests were performed at room temperature at a strain rate of 2.0×10^{-5} s^{-1}, and the tests were repeated more than three times to ensure repeatability. Finally, pseudo-load-controlled tension–tension fatigue tests were conducted using the same tester but with a modified LabView program.[46] The program takes the maximum and minimum desired loads and the frequency as inputs, and proportional control stabilizes load fluctuation as the test progresses. All experimental trials were executed at a load ratio (minimum load/maximum load) of 0.1 and frequency of 5 Hz. It should be noted that the dog-bone shaped samples mounted on the tester were deliberately buckled prior to mechanical testing. This process was done by applying a compressive displacement with the piezo-actuator,
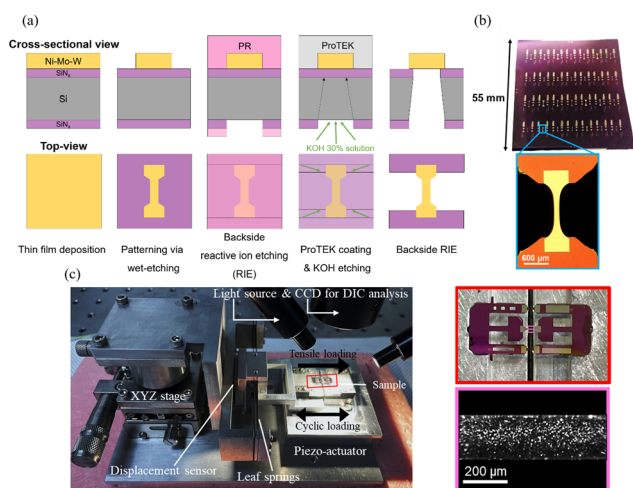

Fig. 1 (a) Stages of fabricating mechanical test specimens starting from thin film sputter deposition. (b) 55 × 55 mm^2 square wafer with 28 dog-bone specimens patterned *via* wet-etching. (c) An overview of the custom-built micro-mechanical tester used for tensile and fatigue tests.

and was executed to eliminate the tensile residual stresses of freestanding Ni–Mo–W thin films that may aggravate the stress concentration effect during cyclic loading.[47]

Results

Texture of Ni–Mo–W thin films before and after annealing

θ–2θ scan XRD diffractograms of as-deposited and annealed Ni–Mo–W are presented in Fig. 2. Ni–Mo–W thin films exhibit a strong (111) out-of-plane texture. In addition, both (111) and (222) peaks have shifted to the left of pure Ni's peaks[48,49] due
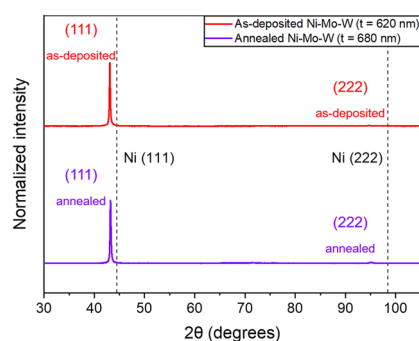

Fig. 2 XRD data of as-deposited (red) and 500 °C × 24 hours annealed (violet) Ni–Mo–W. The dotted lines represent the peak positions of (111) and (222) peaks in pure Ni.

to an increased lattice spacing upon Mo and W addition.[50] There are no visible changes in the XRD data of Ni–Mo–W after annealing at 500 °C for 24 hours; both the peak positions and intensity ratios are virtually identical to those of the as-deposited sample.

Undeformed microstructure of the as-deposited and annealed thin films

The as-deposited Ni–Mo–W (Fig. 3(a)) thin films consist of densely packed columnar grains with an average width of 55 nm (Fig. 3(b)). The vast majority of the grains comprise finely spaced stripes, most of which are slanted with respect to the loading axis; the average deviation from the loading axis is 23.5°, ranging from 2° to 54° (Fig. 3(c)). The cross-sectional micrograph of the annealed sample (Fig. 3(d)) shows columnar grain width and planar fault orientation that are very close to those of the as-deposited sample (Fig. 3(e) and (f)). A closer look at the stripes reveals that the planar fault spacing in both as-deposited and annealed Ni–Mo–W thin films are mostly in angstrom scale (Fig. 4(a) and (c)). The selected area electron diffraction (SAED) patterns of both as-deposited and annealed Ni–Mo–W thin films show intense streaks penetrating the spots, alluding to the high density of SFs (Fig. 4(b) and (d)).

Tensile and fatigue behavior of Ni–Mo–W thin films

The representative stress–strain curves of as-deposited and annealed Ni–Mo–W thin films are plotted in Fig. 5(a). As-de-
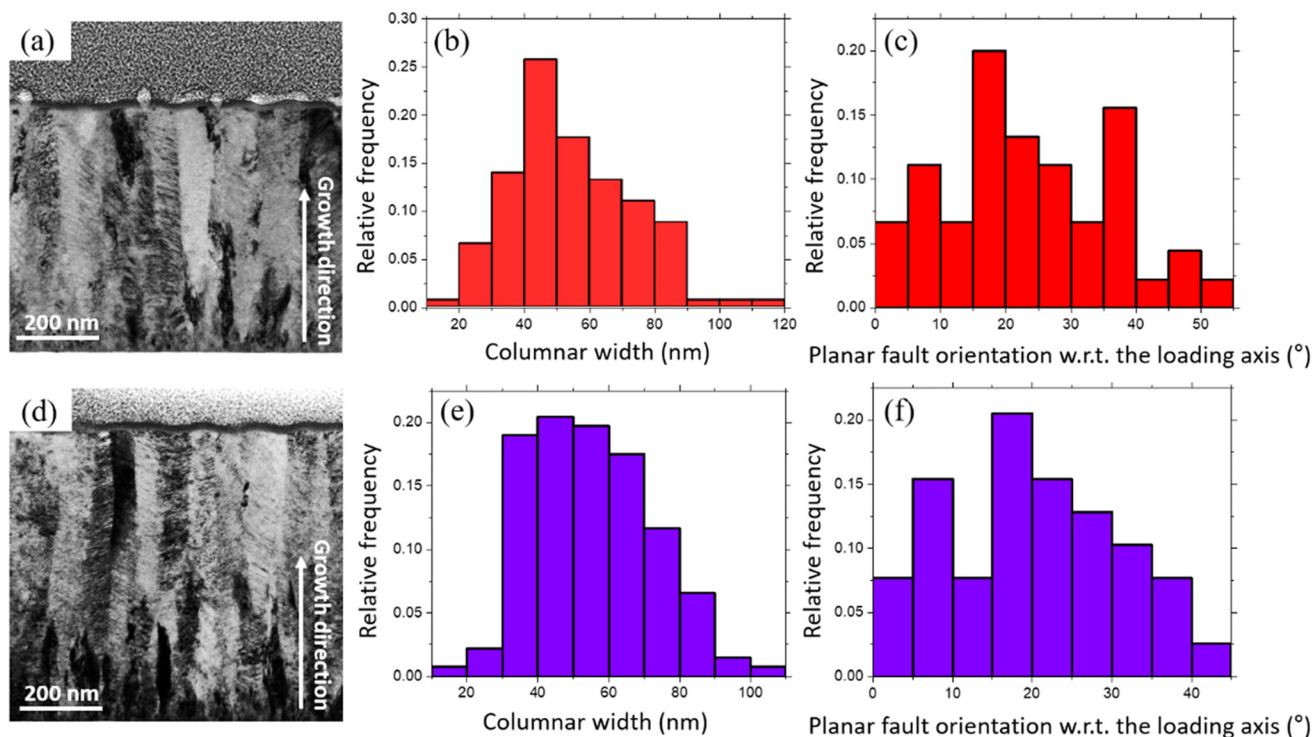

Fig. 3 Cross-sectional BFTEM images of (a) as-deposited, and (d) annealed Ni–Mo–W thin films. Columnar grain width distribution of (b) as-deposited, and (e) annealed specimens. Distribution of planar fault orientation with respect to the loading axis for (c) as-deposited, and (f) annealed specimens.
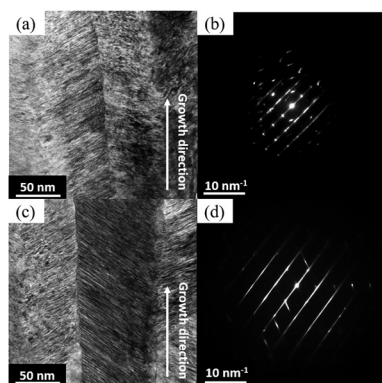
Fig. 4 Cross-sectional BFTEM images focusing on the spacing and orientation of planar faults in (a) as-deposited, and (c) annealed Ni–Mo–W thin films. SAED patterns obtained from heavily-faulted columnar grains in (b) as-deposited, and (d) annealed Ni–Mo–W thin films.

posited Ni–Mo–W thin films show an average tensile strength of 2.83 GPa and an elastic modulus (the initial loading slope) of 170 GPa. The annealed batch has a comparable average tensile strength (2.81 GPa), but the average modulus is slightly higher than that of the as-deposited film (192 GPa). Fig. 5(b) portrays separate sets of tensile test data, in which the films were loaded up to 2600 MPa, fully unloaded, then reloaded until fracture. As-deposited Ni–Mo–W thin film's reloading segment falls between the initial loading and unloading segments, demonstrating an anelastic behavior typically observed in dual-phase steels[51–53] and ufg/nc fcc metal thin films.[42,54–56] Meanwhile, the annealed specimen shows a different mechanical response, where the unloading segment returns to the origin, and the reloading segment coincides with the initial loading path. The implications of anelasticity in the films are elaborated in the Discussion.

Stress-life (S–N) curves of as-deposited and annealed Ni–Mo–W thin films were obtained from tension–tension fatigue tests (Fig. 6(a)). The S–N curves of nc and ufg Ni,[57–60] nc Ni-based alloys,[61–64] and nt Cu-based metallic thin films[65,66] are also plotted together. For clarity, a subset of representative curves has been chosen; S–N curves of all referenced materials can be found in the ESI.† Since the materials of interest were

tested using different load ratios, the stress amplitudes have been adjusted with the modified Goodman relation:

$$S_{a,\text{Goodman}} = \frac{S_a}{\left(1 - \dfrac{S_m}{S_u}\right)}$$

where S_a is the experimental stress amplitude, S_m is the mean stress, and S_u is the ultimate tensile strength (UTS) of the material. As-deposited Ni–Mo–W thin film demonstrates an astounding fatigue strength in the high cycle fatigue (HCF) regime, withstanding over a million cycles of repeated loading at a stress amplitude of 2190 MPa (oscillated between 250 MPa and 2500 MPa). The annealed batch suffers from a sharp decrease in the tolerable stress amplitude with an increase in fatigue life. However, it can still withstand a Goodman stress amplitude of 1050 MPa (oscillated between 160 MPa and 1600 MPa) for over 2×10^5 cycles, enduring stress amplitudes higher than those tested for nt metals, and comparable to those tested for nc Ni-based alloys.

Fig. 6(b) is presented to evaluate whether the superior fatigue behavior of Ni–Mo–W thin films solely originates from their high tensile strengths. The y-axis is the Goodman stress amplitude of the films at 10^5 cycles normalized by their UTS. The tensile and fatigue strengths of all materials in the legend are juxtaposed. As-deposited Ni–Mo–W thin film's normalized fatigue strength is 77%, well above those of nc Ni and nt Cu-based metals spanning from 17 to 54%. Only nc NiFe alloys have similar normalized strengths. Heat treatment has deteriorated the normalized fatigue strength from 77% to 38%, yet the performance is comparable to that of most other metals plotted together. Both Ni–Mo–W thin films possess an excellent combination of tensile and fatigue strengths, and their fatigue strength cannot be simply ascribed to the high tensile strength.

Microstructural analysis of as-deposited Ni–Mo–W thin film after cyclic loading

A portion of as-deposited Ni–Mo–W subjected to 7.8×10^5 cycles, cyclically loaded between 236.5 and 2365 MPa, was lifted-out near the fracture plane for cross-sectional TEM imaging. The columnar grain morphology and its average
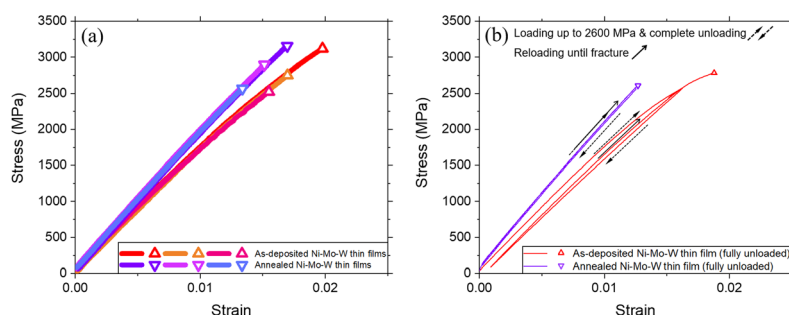

Fig. 5 (a) Representative stress–strain curves of Ni–Mo–W thin films without unloading. (b) Stress–strain curves of Ni–Mo–W thin films that were fully unloaded and reloaded until failure.
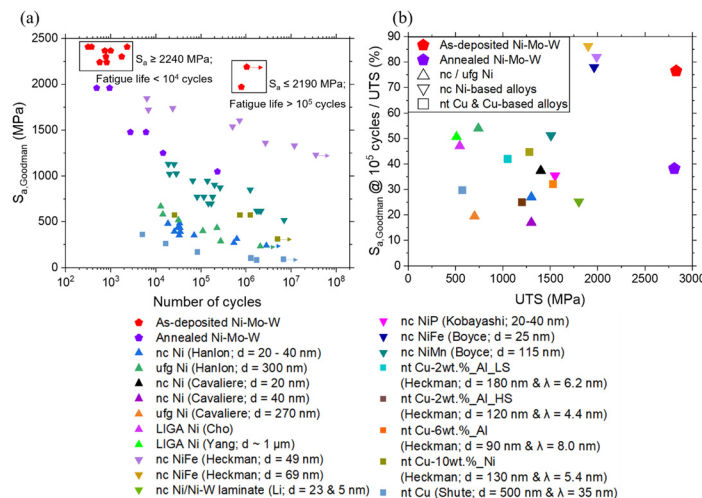
Fig. 6 (a) S–N curves of Ni–Mo–W thin films and reference materials from the literature. (b) Normalized fatigue strength of all reference materials at 10^5 cycles *versus* their UTS. The legend of referenced materials is written in the following format: material type (author's surname; grain size d, TB spacing λ).
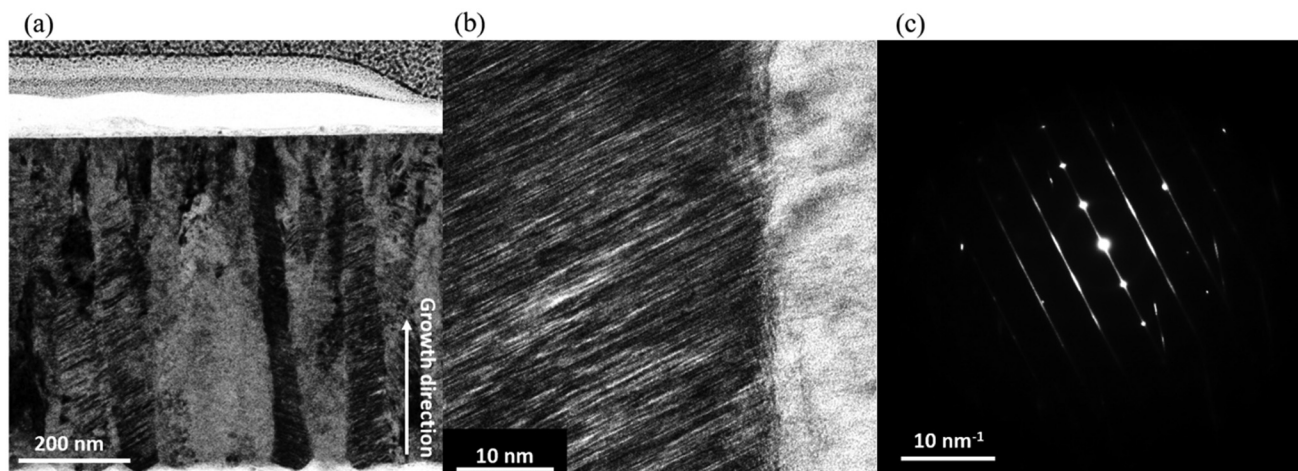

Fig. 7 (a) Cross-section in the vicinity of as-deposited Ni–Mo–W's fracture plane after 7.8×10^5 cycles. (b) HRTEM image focusing on the planar fault configuration. (c) SAED pattern of a heavily-faulted columnar grain.

width were retained (54 ± 13 nm; Fig. 7(a)) after deformation. The same holds for HRTEM images and SAED patterns: planar fault spacing, its misalignment with respect to the loading direction ($23.2 \pm 13.4°$), and the streaks at diffraction spots were unchanged. Similarly, the specimen that fractured after 1001 cycles, cyclically loaded between 260 and 2600 MPa, showed virtually identical characteristics; the columnar grain width was 58 ± 12 nm, and planar fault orientation was $23.2 \pm 10.4°$.

Discussion

General fatigue behavior of Ni–Mo–W thin films

As-deposited Ni–Mo–W thin film exhibits an abrupt transition from high cycle fatigue (HCF; 10^5 cycles or above) to low cycle fatigue (LCF; 10^4 cycles or below) at stress amplitudes of 2240 MPa or above (Fig. 6(a)). Considering that LCF is generally governed by early plastic deformation, the data indicates that significant plastic strain accumulation comes into play at and above that stress level. Annealed Ni–Mo–W on the other hand exhibits a transition from LCF to HCF with a steep gradient. There were no changes in the slope of cyclic load-displacement curves of as-deposited and annealed Ni–Mo–W thin films even when the fracture was imminent (see ESI†), implying that the material did not undergo cyclic hardening or softening. This behavior is in contrast to cyclic hardening and/or softening observed in nc Ni,[67,68] driven by dislocation activities or time-dependent deformation.

Post-mortem characterization of LCF and HCF fractured thin films did not reveal noticeable microstructural changes (Fig. 7). The absence of dislocation activity and other unusual

characteristics near the fracture plane indicates that fatigue failure has occurred in a severely localized manner, such that the responsible deformation mechanism could not come into effect uniformly throughout the microstructure. Based on the aforementioned observations, we can deduce that Ni–Mo–W thin films have excellent crack initiation life at the expense of poor crack propagation life. That is, cracks would propagate instantaneously upon nucleation at a specific "weakest link of the chain" due to localized plastic strain accumulation.

Disparity in the fatigue strengths of as-deposited and annealed specimens

As shown in Fig. 3, there were no conspicuous changes in the texture and microstructure of Ni–Mo–W thin films before and after annealing. A more detailed analysis of the in-plane microstructures of Ni–Mo–W thin films was conducted to examine the presence of nano-scale precipitates. This characterization was deemed necessary as precipitates could exacerbate stress concentration during cyclic loading without adversely affecting the tensile strength.[69] However, no signs of precipitates could be identified in the annealed thin films, and there are no macroscopic changes in the in-plane TEM images and SAED patterns after heat treatment (Fig. 8). The SAED ring patterns only include the indices of fcc Ni, and barely any spots deviate from the rings. Overall, all textural and microstructural characterizations conducted in this work preclude the emergence of precipitates in annealed Ni–Mo–W.

Surface asperities are another commonly reported cause of diminished fatigue strength of metals.[35] If the surface roughness of annealed Ni–Mo–W thin films is higher than that of its as-deposited counterpart, stress concentration would be a logical description of the disparity in the fatigue strength. However, the average roughness (R_a, in nm) values of as-deposited and annealed Ni–Mo–W thin films barely differ (Fig. 9; 4.17 nm for the as-deposited specimen, and 4.16 nm for the annealed specimen). This outcome rules out exacerbated stress concentration in annealed Ni–Mo–W thin films. In view of the above insights, it is more likely that the fatigue strength
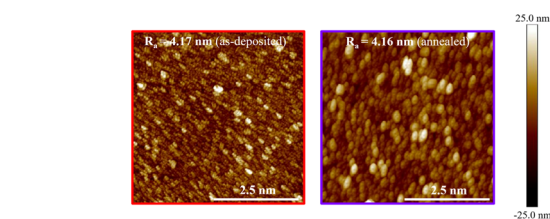

Fig. 9 Surface roughness of as-deposited and annealed samples characterized by AFM.

difference underlies in subtle changes in the microstructure and the resultant deformation mechanisms.

Possible fatigue failure mechanisms of Ni–Mo–W thin films

Nano-scale columnar grains and angstrom-scale planar faults would serve as powerful obstacles to dislocation movement in Ni–Mo–W thin films. In particular, both TBs and SFs offer pronounced strengthening as the spacing reduces down to a few nanometers.[15,72,73] Impeding dislocation movement effectively delays fatigue crack initiation, and this suitably explains the superb crack initiation life of Ni–Mo–W thin films over the materials juxtaposed in Fig. 6. The poor crack propagation life can be conveniently rationalized by the macroscopically brittle behavior, but the detailed microscopic picture is unknown at this stage. Though the lack of microstructural changes after deformation obscures an accurate analysis, this section conjectures various deformation mechanisms in cyclically loaded Ni–Mo–W thin films based on analogous studies.

Incompatibility in dislocation–planar fault interactions. The spacings and inclination angles of the planar faults in Ni–Mo–W are non-uniform (Fig. 3 and 10(a)), which may have activated different dislocation-based mechanisms. For instance, nanotwins aligned parallel to unidirectional loading undergo a shift in the deformation mechanism as the TB spacing is reduced.[12,15,72] A nanotwinned metal with TB spacing between 10 and 100 nm deforms by threading dislocation motion confined between the TBs,[15] whereas that with TB spacing below 10 nm deforms by collective motion of jogged dislocations.[72] The latter mechanism is known to strengthen the metal more effectively than the former. Thus, the planar faults separated by a distance over 10 nm in Ni–Mo–W (Fig. 10(a)) would be incapable of accommodating high stresses compared to those separated within a few atomic layers. The inclination angle of planar faults also plays an analogous role. Pan *et al.* studied the history-independent cyclic behavior of nt Cu and attributed the behavior to the reversible movement of correlated necklace dislocations (CNDs).[71] The authors emphasized that the aforementioned mechanism holds only when the nanotwins are tilted within 15 degrees with respect to the loading axis. That is, cyclic deformation is no longer purely governed by the movement of CNDs when the misalignment exceeds 15 degrees, which results in an irreversible cyclic damage. Applying this argument to Ni–Mo–W thin films, severely slanted planar faults may have functioned as vulnerable sites
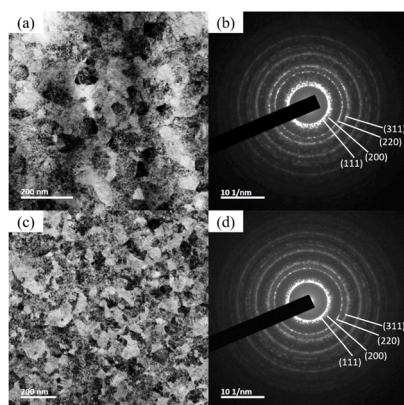

Fig. 8 (a) & (b) In-plane TEM image of as-deposited Ni–Mo–W and the polycrystal's SAED pattern. (c) & (d) Equivalent images of annealed Ni–Mo–W.

(a) **Deformation incompatibility** (b) **Fatigue-induced de-faulting** (c) **Grain boundary cracking**
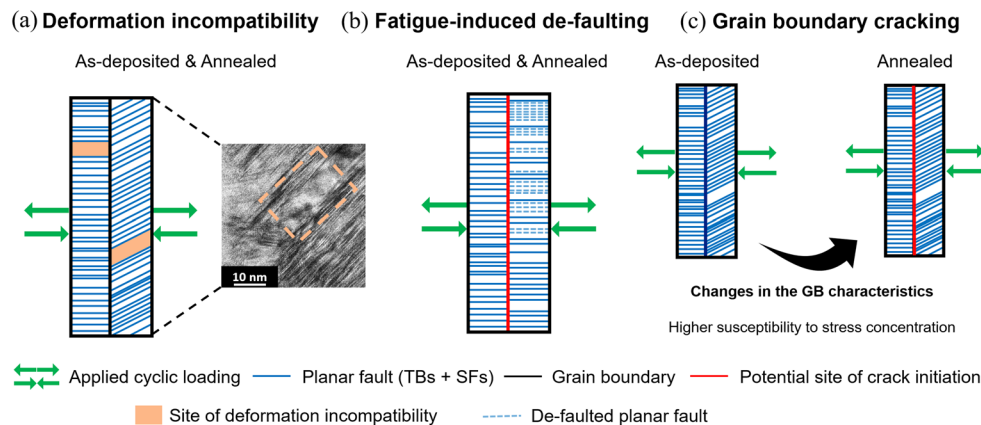

Fig. 10 Schematics of potential failure mechanisms. (a) Deformation incompatibility due to variations in the planar fault configuration. (b) Crack nucleation between a densely-faulted grain and a de-faulted grain. (c) GB cracking from intensified GB sliding upon strain accumulation, driven by changes in the GB characteristics after annealing.

under cyclic loading. Overall, deformation incompatibility due to variations in the planar fault spacing and/or inclination angle of planar faults in Ni–Mo–W could lead to premature failure at the weakest region (Fig. 10(a)).

Fatigue-induced loss of planar faults (de-faulting). Two independent case studies[65,66] on columnar-grained nanotwinned Cu and Cu-based alloy films discovered that the films lost a portion of twinned grains under cyclic loading parallel to the TB orientation. Eventually, the films fractured from fatigue cracks that had initiated at an intersection between a det-winned grain and a harder interface: the free surface,[66] and a fully twinned grain.[65] Shute et al.[66] established that samples subjected to tension–tension cyclic loading underwent severe detwinning, which has been attributed to the motion of ledges. On the other hand, films subjected to compressive modes of loading underwent only minuscule detwinning. Heckman et al.[65] also remarked that tension–tension cyclic deformation mechanism switches from slip band formation to detwinning as the TB spacing is reduced down to 35 nm or below. This transition concurs with the trend that detwinning occurs more easily in materials with finer TB spacing.[14] Besides the two preceding studies, Pan et al.[70] claimed that sufficiently large columnar grain width – 6 μm in their nanotwinned Cu with average TB spacing of 78 nm – minimized detwinning by providing sufficient room for threading dislocation motion. Combining these insights, Ni–Mo–W's sub-nanometer planar fault spacing and nano-scale columnar grains may favor fatigue-mediated de-faulting especially under tension–tension cyclic loading, and this could have facilitated crack nucleation between the inhomogeneous columnar grains (Fig. 10(b)).

Grain boundary (GB)-mediated plasticity. Alternatively, fatigue failure in Ni–Mo–W thin films may have transited from dislocation–planar fault interaction at lower strains to GB plasticity prior to fracture. Fang and Sansoz[74] conducted MD simulations to examine GB plasticity in columnar-grained nt fcc metals under uniaxial tension applied parallel to the TB orien-

tation. The authors discovered that nt Cu, Ag, and Al exhibited continuous strengthening as the TB spacing was reduced down to 1.2 nm, adhering to the model of threading and jog dislocation movement. In contrast, the deformation mechanism in nt Ni shifted from dislocation activity to GB sliding at TB spacings below 6.02 nm and tensile strains above 2%. GB sliding in nt Ni was ascribed to large free volume at the GBs, which subsequently drives micro-void formation and coalescence. Ni–Mo–W is a Ni-based solid solution system with an average planar fault spacing much finer than 6.02 nm, meeting the requirements for GB plasticity introduced in the reference. Additionally, Ni–Mo–W thin film's low elastic modulus (compared to that of (111) textured pure Ni; 232 GPa (ref. 75)) and anelastic behavior (Fig. 5(a) and (b)) reinforce GB sliding as a viable deformation mechanism.[42,55,56,76] Thus, strain accumulation developed in Ni–Mo–W during cyclic loading could have activated GB plasticity-mediated cracking rather than dislocation-mediated failure (Fig. 10(c)).

Overall evaluation of the hypotheses. The "most likely" postulate among those listed in the Discussion can be pinpointed by focusing on the fatigue strength gap between the as-deposited and annealed Ni–Mo–W thin films. Though high-density planar faults in both types of Ni–Mo–W thin films contribute to delaying the fatigue crack initiation, postulates based on planar fault–dislocation interactions cannot elucidate the aforementioned gap. This is because the cross-sectional micrographs of as-deposited and annealed Ni–Mo–W portray virtually identical grain morphology and planar fault configuration. In other words, unless there was annealing-induced de-faulting that could not be identified from the observations in this study, as-deposited and annealed Ni–Mo–W thin films should possess comparable fatigue strengths.

On the other hand, the GB plasticity postulate can partially explain the gap. The mechanical response of Ni–Mo–W after annealing (Fig. 5(b)) implies that there were changes in the GB characteristics. One notable feature could be the presence of band-like or elliptical/granular nano-scale amorphous phases

in the as-deposited films (Fig. S4†). The amorphous regions were identified along or near the GBs of as-deposited thin films, as illustrated in the ESI.† It is widely accepted that amorphous GB phases release shear stress accumulation by promoting GB sliding,[77–79] and they are also known to promote steady fatigue crack growth and even plasticity distribution by diffusing the strain concentration at the GBs.[80,81] Conversely, no evidence of similar nanostructures could be found in the micrographs of annealed Ni–Mo–W thin films. The lack of strain-accommodating regions could be a source of expedited stress concentration at the GBs of annealed thin films, but the scarcity of clear amorphous phases in the as-deposited films blurs a definitive analysis. Nevertheless, there could be room for annealing-induced changes in the GB characteristics in Ni–Mo–W thin films. Studies on the thermal stability of Ni–Mo–W systems characterized the structural evolution of GBs during heat-treatment at intermediate temperatures (400 °C to 800 °C).[33,82] These studies revealed GB migration in $Ni_{85}Mo_{13}W_2$ thin film annealed at 400 °C,[33] and GB relaxation in $Ni_{79.4}Mo_{17}W_{3.6}$ annealed at 525 °C and above.[82] Considering these insights, we surmise that GBs in annealed Ni–Mo–W thin films can undergo structural evolution at a microscopic level. An in-depth characterization of the GBs in as-deposited and annealed Ni–Mo–W thin films will be conducted to shed light on the discrepancy, and how the discrepancy affects Ni–Mo–W thin film's susceptibility to stress concentration driven by cyclic loading.

Conclusion

This study investigated the fatigue behavior of freestanding sputter-deposited Ni–Mo–W thin films by conducting pseudo-load-controlled tension–tension fatigue tests and analyzing the microstructure. As-deposited films showed an extraordinary fatigue strength, lasting over 10^6 cycles at a Goodman stress amplitude of 2190 MPa. The microstructure of Ni–Mo–W remained robust even after cyclic deformation and annealing at 500 °C for 24 hours. The fatigue life of Ni–Mo–W has deteriorated after annealing, but it still exceeds 2×10^5 cycles at a Goodman stress amplitude of 1050 MPa. Plausible origins of Ni–Mo–W's superb fatigue behavior were delineated in terms of planar fault–dislocation interactions and GB plasticity. Both hypotheses are justifiable accounts of fatigue failure in Ni–Mo–W, but the GB plasticity postulate better explains the fatigue strength disparity between the as-deposited and annealed specimens. The GB plasticity postulate links the disparity with structural evolution of GBs upon annealing, rendering the GBs in the annealed thin films more susceptible to stress concentration. A detailed TEM analysis is to be undertaken to substantiate this hypothesis. Ni–Mo–W thin films were already recognized for their high unidirectional strengths as well as thermal and mechanical stability, but this study consolidated their potential as nano-scale structural components by evaluating the reliability under fatigue. Further investigation could reveal whether Ni–Mo–W retains a similar level of fatigue performance under cyclic loading at elevated temperatures, and whether the responsible mechanism changes.

Author contributions

JungHun Park: conceptualization, investigation, validation, writing – original draft, writing – review & editing. Yuhyun Park: investigation, methodology, resources, writing – review & editing. Sunkun Choi: methodology, software, writing – review & editing. Zhuo Feng Lee: formal analysis, methodology, writing – review & editing. Gi-Dong Sim: conceptualization, funding acquisition, supervision, writing – review & editing.

Conflicts of interest

There are no conflicts to declare.

Acknowledgements

References

1 K. Lu, L. Lu and S. Suresh, *Science*, 2004, **324**, 349–352.
2 L. Lu, X. Chen, X. Huang and K. Lu, *Science*, 2009, **323**, 607–610.
3 L. Lu, Y. Shen, X. Chen, L. Qian and K. Lu, *Science*, 2004, **304**, 422–426.
4 R. T. Ott, J. Geng, M. F. Besser, M. J. Kramer, Y. M. Wang, E. S. Park, R. Lesar and A. H. King, *Acta Mater.*, 2015, **96**, 378–389.
5 C. Deng and F. Sansoz, *Acta Mater.*, 2009, **57**, 6090–6101.
6 X. Ke, J. Ye, Z. Pan, J. Geng, M. F. Besser, D. Qu, A. Caro, J. Marian, R. T. Ott, Y. M. Wang and F. Sansoz, *Nat. Mater.*, 2019, **18**, 1207–1214.
7 O. Anderoglu, A. Misra, H. Wang and X. Zhang, *J. Appl. Phys.*, 2008, **103**(9), DOI: **10.1063/1.2913322**.
8 Y. Wang, E. Ma, R. Z. Valiev and Y. Zhu, *Adv. Mater.*, 2004, **16**, 328–331.
9 Y. Zhao, T. A. Furnish, M. E. Kassner and A. M. Hodge, *J. Mater. Res.*, 2012, **27**, 3049–3057.
10 D. Jang, C. Cai and J. R. Greer, *Nano Lett.*, 2011, **11**, 1743–1746.
11 A. M. Hodge, T. A. Furnish, C. J. Shute, Y. Liao, X. Huang, C. S. Hong, Y. T. Zhu, T. W. Barbee and J. R. Weertman, *Scr. Mater.*, 2012, **66**, 872–877.
12 K. Lu, *Nat. Rev. Mater.*, 2016, **1**, 16019.
13 Z. S. You, L. Lu and K. Lu, *Acta Mater.*, 2011, **59**, 6927–6937.

14 J. Wang, N. Li, O. Anderoglu, X. Zhang, A. Misra, J. Y. Huang and J. P. Hirth, *Acta Mater.*, 2010, **58**, 2262–2270.

15 Z. You, X. Li, L. Gui, Q. Lu, T. Zhu, H. Gao and L. Lu, *Acta Mater.*, 2013, **61**, 217–227.

16 X. Li, Y. Wei, L. Lu, K. Lu and H. Gao, *Nature*, 2010, **464**, 877–880.

17 T. Zhu and H. Gao, *Scr. Mater.*, 2012, **66**, 843–848.

18 D. Jang, X. Li, H. Gao and J. R. Greer, *Nat. Nanotechnol.*, 2012, **7**, 594–601.

19 R. Su, D. Neffati, Y. Zhang, J. Cho, J. Li, H. Wang, Y. Kulkarni and X. Zhang, *Mater. Sci. Eng., A*, 2021, **803**, 140696.

20 X. Feng, J. Zhang, K. Wu, X. Liang, G. Liu and J. Sun, *Nanoscale*, 2018, **10**, 13329–13334.

21 R. Su, D. Neffati, S. Xue, Q. Li, Z. Fan, Y. Liu, H. Wang, Y. Kulkarni and X. Zhang, *Mater. Sci. Eng., A*, 2018, **736**, 12–21.

22 J. Li, J. Cho, J. Ding, H. Charalambous, S. Xue, H. Wang, X. Li Phuah, J. Jian, X. Wang, C. Ophus, T. Tsakalakos, R. Edwin García, A. K. Mukherjee, N. Bernstein, C. Stephen Hellberg, H. Wang and X. Zhang, *Sci. Adv.*, 2019, **5**, eaaw5519.

23 D. Zhang, J. Zhang, T. Xu, Y. Zhang, C. Che, D. Zhang and J. Meng, *Mater. Sci. Eng., A*, 2022, **845**, 143238.

24 W. W. Jian, G. M. Cheng, W. Z. Xu, H. Yuan, M. H. Tsai, Q. D. Wang, C. C. Koch, Y. T. Zhu and S. N. Mathaudhu, *Mater. Res. Lett.*, 2013, **1**, 61–66.

25 C. A. C. Sequeira, D. S. P. Cardoso, L. Amaral, B. Šljukić and D. M. F. Santos, *Corros. Rev.*, 2016, **34**, 187–200.

26 M. Pröbstle, S. Neumeier, J. Hopfenmüller, L. P. Freund, T. Niendorf, D. Schwarze and M. Göken, *Mater. Sci. Eng., A*, 2016, **674**, 299–307.

27 G.-D. Sim, J. A. Krogstad, K. M. Reddy, K. Y. Xie, G. M. Valentino, T. P. Weihs and K. J. Hemker, *Sci. Adv.*, 2017, **3**, e1700685.

28 G.-D. Sim, J. A. Krogstad, K. Y. Xie, S. Dasgupta, G. M. Valentino, T. P. Weihs and K. J. Hemker, *Acta Mater.*, 2018, **144**, 216–225.

29 Y. Park, S. Choi, K.H. Ryou, JH. Park, W. S. Choi, W.-S. Ko, P.-P. Choi and G.-D. Sim, manuscript in preparation.

30 G. M. Valentino, P. P. Shetty, A. Chauhan, J. A. Krogstad, T. P. Weihs and K. J. Hemker, *Scr. Mater.*, 2020, **186**, 247–252.

31 G. M. Valentino, J. A. Krogstad, T. P. Weihs and K. J. Hemker, *J. Alloys Compd.*, 2020, **833**, 155024.

32 K. Kim, S. Park, T. Kim, Y. Park, G.-D. Sim and D. Lee, *J. Alloys Compd.*, 2022, **919**, 165808.

33 M. R. He, R. Zhang, R. Dhall, A. M. Minor and K. J. Hemker, *Mater. Res. Lett.*, 2023, **11**, 879–887.

34 G. M. Valentino, P. P. Shetty, J. A. Krogstad and K. J. Hemker, *J. Microelectromech. Syst.*, 2020, **29**, 329–337.

35 R. I. Stephens and H. O. Fuchs, *Metal fatigue in engineering*, Wiley, 2001.

36 M. M. Saleem and H. Nawaz, *Micro Nanosyst.*, 2019, **11**, 11–33.

37 R. Schwaiger and O. Kraft, *Acta Mater.*, 2003, **51**, 195–206.

38 B. Merle and M. Göken, *J. Mater. Res.*, 2014, **29**, 267–276.

39 T. Kondo, X. C. Bi, H. Hirakata and K. Minoshima, *Int. J. Fatigue*, 2016, **82**, 12–28.

40 A. Barrios, C. Kunka, J. Nogan, K. Hattar and B. L. Boyce, *Small Methods*, 2023, 7(7), 2201591.

41 H. D. Espinosa, B. C. Prorok and M. Fischer, *A methodology for determining mechanical properties of freestanding thin ÿlms and MEMS materials*, 2003, vol. 51.

42 H. Kim, J.-H. Choi, Y. Park, S. Choi and G.-D. Sim, *J. Mech. Phys. Solids*, 2023, **173**, 105209.

43 Z. F. Lee, H. Ryu, J.-Y. Kim, H. Kim, J.-H. Choi, I. Oh and G.-D. Sim, *Mater. Sci. Eng., A*, 2024, **892**, 146028, DOI: **10.1016/j.msea.2023.146028**.

44 G.-D. Sim, J. H. Park, M. D. Uchic, P. A. Shade, S. B. Lee and J. J. Vlassak, *Acta Mater.*, 2013, **61**, 7500–7510.

45 C. Eberl, R. Thompson, D. Gianola and S. Bundschuh, *Digital Image Correlation and Tracking with Matlab*, 2012.

46 S. Choi, J. H. Park, Y. Park, H. Ryu, Z. F. Lee and G.-D. Sim, manuscript in preparation.

47 G. A. Webster and A. N. Ezeilo, *Int. J. Fatigue*, 2001, **23**, 375–383.

48 B. Geetha Priyadarshini, S. Aich and M. Chakraborty, *Bull. Mater. Sci.*, 2014, **37**, 1265–1273.

49 C. Xiao, R. A. Mirshams, S. H. Whang and W. M. Yin, *Mater. Sci. Eng., A*, 2001, **301**, 35–43.

50 W. Nix and W. Cai, *Imperfections in Crystalline Solids*, Cambridge University Press, 1st edn, 2016.

51 D. Li and R. H. Wagoner, *Acta Mater.*, 2021, **206**, 116625.

52 H. Kim, C. Kim, F. Barlat, E. Pavlina and M. G. Lee, *Mater. Sci. Eng., A*, 2013, **562**, 161–171.

53 E. J. Pavlina, M. G. Lee and F. Barlat, *Metall. Mater. Trans. A*, 2015, **46**, 18–22.

54 R. P. Vinci, G. Cornella and J. C. Bravman, *AIP*, 2011, pp. 240–248.

55 G.-D. Sim and J. J. Vlassak, *Scr. Mater.*, 2014, **75**, 34–37.

56 I. Oh, H. Kim, H. Son, S. Nam, H. Choi and G.-D. Sim, *Int. J. Plast.*, 2023, 161, DOI: **10.1016/j.ijplas.2023.103515**.

57 T. Hanlon, Y. N. Kwon and S. Suresh, *Scr. Mater.*, 2003, **49**, 675–680.

58 P. Cavaliere, *Int. J. Fatigue*, 2009, **31**, 1476–1489.

59 H. S. Cho, K. J. Hemker, K. Lian and J. Goettert, Technical Digest, in *MEMS 2002 IEEE International Conference*.

60 Y. Yang, B. I. Imasogie, S. M. Allameh, B. Boyce, K. Lian, J. Lou and W. O. Soboyejo, *Mater. Sci. Eng., A*, 2007, **444**, 39–50.

61 N. M. Heckman, H. A. Padilla, J. R. Michael, C. M. Barr, B. G. Clark, K. Hattar and B. L. Boyce, *Int. J. Fatigue*, 2020, **134**, 105472.

62 M. Y. Li, Z. X. Wang, B. Zhang, F. Liang, X. M. Luo and G. P. Zhang, *Scr. Mater.*, 2023, **222**, 114995.

63 S. Kobayashi, A. Kamata and T. Watanabe, in *Journal of Physics: Conference Series*, Institute of Physics Publishing, 2010, vol. 240.

64 B. L. Boyce and H. A. Padilla, *Metall. Mater. Trans. A*, 2011, **42**, 1793–1804.

65 N. M. Heckman, M. F. Berwind, C. Eberl and A. M. Hodge, *Acta Mater.*, 2018, **144**, 138–144.

66 C. J. Shute, B. D. Myers, S. Xie, S. Y. Li, T. W. Barbee, A. M. Hodge and J. R. Weertman, *Acta Mater.*, 2011, **59**, 4569–4577.

67 B. Moser, T. Hanlon, K. S. Kumar and S. Suresh, *Scr. Mater.*, 2006, **54**, 1151–1155.

68 S. Cheng, J. Xie, A. D. Stoica, X. L. Wang, J. A. Horton, D. W. Brown, H. Choo and P. K. Liaw, *Acta Mater.*, 2009, **57**, 1272–1280.

69 K. Hockauf, M. F. X. Wagner, T. Halle, T. Niendorf, M. Hockauf and T. Lampke, *Acta Mater.*, 2014, **80**, 250–263.

70 Q. S. Pan, Q. H. Lu and L. Lu, *Acta Mater.*, 2013, **61**, 1383–1393.

71 Q. S. Pan, H. Zhou, Q. Lu, H. Gao and L. Lu, *Nature*, 2017, **551**, 214–217.

72 H. Zhou, X. Li, S. Qu, W. Yang and H. Gao, *Nano Lett.*, 2014, **14**, 5075–5080.

73 W. W. Jian, G. M. Cheng, W. Z. Xu, C. C. Koch, Q. D. Wang, Y. T. Zhu and S. N. Mathaudhu, *Appl. Phys. Lett.*, 2013, **103**, 133108, DOI: **10.1063/1.4822323**.

74 Q. Fang and F. Sansoz, *Acta Mater.*, 2021, **212**, 116925.

75 H. M. Ledbetter and R. P. Reed, *J. Phys. Chem. Ref. Data*, 1973, **2**, 531–618.

76 A. J. Kalkman, A. H. Verbruggen and G. C. A. M. Janssen, *Appl. Phys. Lett.*, 2001, **78**, 2673–2675.

77 S. Guo and H. Sun, *Acta Mater.*, 2021, **218**, 117212, DOI: **10.1016/j.actamat.2021.117212**.

78 K. Madhav Reddy, J. J. Guo, Y. Shinoda, T. Fujita, A. Hirata, J. P. Singh, J. W. McCauley and M. W. Chen, *Nat. Commun.*, 2012, **3**, 1052, DOI: **10.1038/ncomms2047**.

79 I. Szlufarska, A. Nakano and P. Vashishta, *Science*, 2005, **309**, 911–913.

80 A. Khalajhedayati, Z. Pan and T. J. Rupert, *Nat. Commun.*, 2016, **7**, 10802, DOI: **10.1038/ncomms10802**.

81 J. D. Schuler, C. M. Barr, N. M. Heckman, G. Copeland, B. L. Boyce, K. Hattar and T. J. Rupert, *JOM*, 2019, **71**, 1221–1232.

82 D. Zeng, J. Li, Y. Shi, X. Li and K. Lu, *Nano Res.*, 2023, **16**, 12800–12808.